

Wind/WAVES Instrument and Data Analysis

Lynn B. Wilson III

December 8, 2010

Contents

1	Introduction	4
2	WAVES	4
2.1	Time Domain Sampler Receiver	6
2.1.1	Langmuir Waves	8
2.1.2	Ion-Acoustic Waves	10
2.1.3	Electrostatic Solitary Waves	13
2.1.4	Whistler Waves	16
2.1.5	Waves at or Near the Electron Cyclotron Frequency	20
2.1.6	Lower Hybrid Waves	23
2.2	Magnetic Field Rotations	28
2.2.1	Radio Receivers	28
3	SCET Corrections	29

List of Figures

1	Wind Spacecraft Coordinates	5
2	Wind Spacecraft Rotations and B-field	7
3	Wind TDS Rotation Example	9
4	Example Langmuir Wave	11
5	Example Ion Acoustic Wave	12
6	Example Solitary Wave	15
7	Example Precursor Whistler Wave	17
8	Example Whistler Waves	18
9	Example Electron Cyclotron Waves	22
10	Example Lower Hybrid Wave	24
11	Example Lower Hybrid Wave: Low Frequency Filter	26
12	Example Lower Hybrid Wave: High Frequency Filter	27

List of Tables

1	Wind WAVES TDS Specs	8
2	Wind WAVES TNR Specs	29

1 Introduction

The Wind spacecraft was launched on November 1st, 1994 by a Delta II rocket from Cape Canaveral Air Force Station in Merritt Island, FL. For the first two years of the mission WIND was in a highly elliptical orbit on the sunward side of the Earth with an apogee of 250 Earth radii (R_E) and a perigee of at least 5 R_E . Wind is the first of NASA's Global Geospace Science (GGS) program, which is part of the International Solar-Terrestrial Physics (ISTP) Science Initiative, a collaboration between several countries in Europe, Asia, and North America. The aim of ISTP is to understand the behavior of the solar-terrestrial plasma environment in order to predict how the Earth's atmosphere will respond to changes in solar wind conditions. WIND's objective is to measure the properties of the solar wind before it reaches the Earth [Desch, 2005].

The Wind spacecraft has an array of instruments including: Konus [Aptekar *et al.*, 1995], the Wind Magnetic Field Investigation (MFI) [Lepping *et al.*, 1995], the Solar Wind and Suprathermal Ion Composition Experiment (SMS) [Gloeckler *et al.*, 1995], the Solar Wind Experiment (SWE) [Ogilvie *et al.*, 1995], a Three-Dimensional Plasma and Energetic Particle Investigation (3DP) [Lin *et al.*, 1995], the Transient Gamma-Ray Spectrometer (TGRS) [Owens *et al.*, 1995], and the Radio and Plasma Wave Investigation (WAVES) [Bougeret *et al.*, 1995]. The Konus and TGRS instruments are primarily for gamma-ray and high energy photon observations of solar flares or gamma-ray bursts. The SMS experiment measures the mass and mass-to-charge ratios of heavy ions. The SWE and 3DP experiments are meant to measure/analyze the lower energy (below 10 MeV) solar wind protons and electrons. The WAVES and MFI experiments were designed to measure the electric and magnetic fields observed in the solar wind. All together, the Wind spacecrafts suite of instruments allows for a complete description of plasma phenomena in the solar wind plane of the ecliptic [Desch, 2005].

2 WAVES

The electric field detectors of the Wind WAVES instrument [Bougeret *et al.*, 1995] are composed of three orthogonal electric field dipole antenna, two in the spin plane (roughly the plane of the ecliptic) of the spacecraft and one along the spin axis. The complete WAVES suite of instruments includes five total receivers including: Low Frequency FFT receiver called FFT (0.3 Hz to 11 kHz), Thermal Noise Receiver called TNR (4-256 kHz), Radio receiver band 1 called RAD1 (20-1040 kHz), Radio receiver band 2 called RAD2

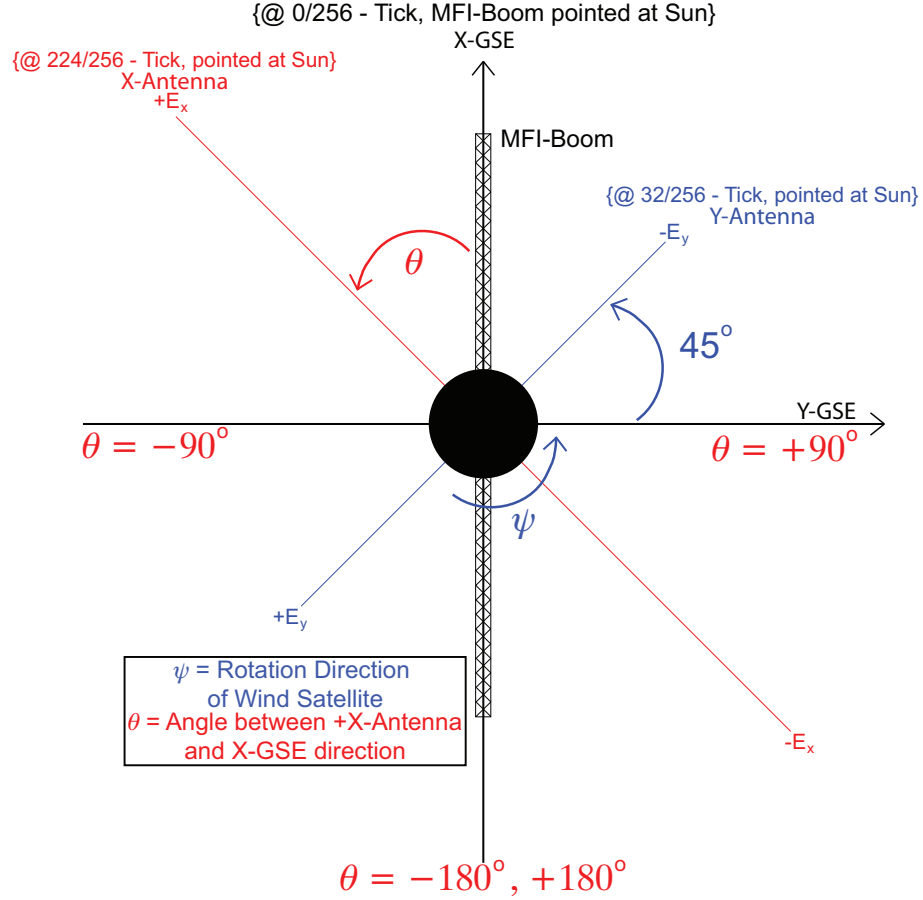


Figure 1: This is a schematic cartoon used to illustrate the relationship between the various field instruments on the Wind spacecraft and the GSE-coordinate system. The relative angles are determined by an eight bit integer. As seen in the image, when this integer equals zero, the magnetic field boom (the x-framed boom along the X-GSE axis) is pointed towards the sun (X-GSE). When the integer reads 224, the positive X-antenna (electric field, E_x) is pointed towards the sun. The magnetic field boom is roughly 45° from either X (red line) or Y-antenna (blue line). As indicated by the figure, the satellite rotates in a counter-clockwise direction in this coordinate system.

(1.075-13.825 MHz), and the Time Domain Sampler called TDS (≤ 7.5 kHz in slow mode and ≤ 120 kHz in fast mode). The longer of the two spin plane antenna, defined as E_x , is 100 m tip-to-tip while the shorter, defined as E_y , is 15 m tip-to-tip. The spin axis dipole, defined as E_z , is roughly 12 m tip-to-tip. When accounting for spacecraft potential, these antenna lengths are adjusted to ~ 41.1 m, ~ 3.79 m, and ~ 2.17 m, respectively (P.J. Kellogg, Personal Communication, 2007). The magnetic field detectors of the Wind WAVES instrument are composed of three orthogonal search coil magnetometers (designed and built by the University of Iowa). The XY search coils are oriented to be parallel to the XY dipole antenna. Thus, in Figure 1, the X-component search coil is at an angle θ from the X-GSE direction. The search coils allow for high frequency magnetic field measurements (defined as B_x , B_y , and B_z). The WAVES Z-Axis is anti-parallel to Z-GSE direction. Thus any rotations can be done about the Z-Axis in the normal Eulerian sense followed by a change of sign in the Z-component of any GSE vector rotated into WAVES coordinates.

Figure 1 is a schematic used to illustrate the relationship between the various field instruments on the Wind spacecraft and the GSE-coordinate system. The point of view is from the negative Z-GSE direction (*i.e.* below the plane of the ecliptic) looking toward the positive Z-GSE direction (*i.e.* above the plane of the ecliptic). The spacecraft rotates in a counterclockwise direction in this coordinate system. The house keeping information which informs a user where each boom is with respect to the sun direction is returned as an eight bit integer, providing $\sim 1.5^\circ$ accuracy. The angle θ is relevant to the software which retrieves TDS samples from the VAX/ALPHA systems (see Section 2.1).

2.1 Time Domain Sampler Receiver

Electric (and magnetic) field waveform captures can be obtained from the Time Domain Sampler (TDS) receiver [Bougeret *et al.*, 1995]. In the highest sampling rates, the TDS samples are ~ 17 ms waveform capture of 2048 points (120 kHz) for the Fast (TDSF) sampler and 7.5 kHz for the Slow (TDSS) sampler. The TDS receiver has four possible modes (see Table 1). In the solar wind, TDSF is usually set to sample in the 120 kHz mode but was changed to the 7.5 or 1.9 kHz modes during the petal orbits through the Earth's magnetosphere. TDSF samples (see Figure 3) are two components of the electric field (typically in the XY-GSE plane), defined as E_x and E_y (occasionally chosen to be E_z prior to 1996). For TDSF samples, we define $|E_{xy}| = \sqrt{E_x^2 + E_y^2}$ as the peak-to-peak (pk-pk) amplitude of the waveform. When operating at 120 kHz, the TDSF receiver has little to no gain below ~ 120 Hz, thus the data is cutoff below 150 Hz when performing gain corrections

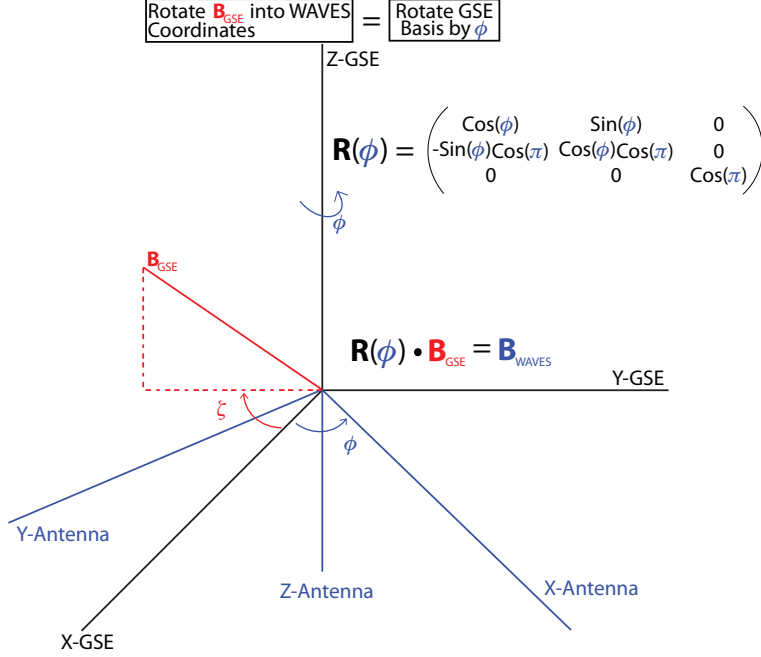


Figure 2: This is a schematic cartoon used to illustrate the rotation from a GSE basis to the WAVES antenna basis. The Z-component of the magnetic field must change a sign after rotation about the Z-GSE axis. The figure shows a rotation about the Z-Axis by an angle ϕ (blue) which results in the X-antenna aligning with the new X'-Axis. The X'Y'-projection of the magnetic field in this basis is the rotated field one uses when plotting hodograms of the electric field from WAVES.

on ground (P.J. Kellogg, Personal Communication, 2007). Nearly all of the data presented in this thesis is from the TDSF receiver.

Figure 2 is a schematic cartoon used to illustrate an example rotation from the GSE basis to the WAVES antenna basis. The blue lines represent the WAVES basis at rotated about the negative Z-GSE axis by an angle ϕ . The angle ζ represents the angle between the projection of the magnetic field in GSE coordinates (\mathbf{B}_{GSE}) onto the XY-GSE plane and the X-GSE axis. The rotation matrix given in the figure will rotate \mathbf{B}_{GSE} into WAVES coordinates resulting in, \mathbf{B}_{WAVES} . This is calculation necessary for analysis of wave polarizations. Also, for lower sampling rates (*e.g.* ≤ 7.5 kHz), this rotation should be done on each data point since the angle ϕ can change by up to $\sim 120^\circ$ during on TDS sample when sampling at 1875

Table 1: Wind WAVES TDS Specs

Speed	Fast Sampler (sps)	Slow Sampler (sps)
A	120,000	
B	30,000	
C	7,500	7,500
D	1,875	1,875
E		468
F		117

Hz.

The TDSS samples return 4 field vectors, either three electric and one magnetic or one magnetic and three electric field measurements. The TDSS receiver also has four possible sample rates, as shown in Table 1 from *Bougeret et al.* [1995]. The gain for the TDSS search coils rolls off below 3.3 Hz. When returning three electric fields, the TDSS samples are often contaminated by spin effects due to different levels of photoelectron currents on the antenna in sunlight versus shadow (*i.e.* only affects the X and Y components) and a glitch associated with the Z-antenna (P.J. Kellogg, Personal Communication, 2007). However, if the electric fields are large enough and Wind is in the shadow of the Earth, these effects are negligible. When returning three magnetic and one electric field, the TDSS receiver can return well defined waveforms with only small noise and glitch effects. The TDSS receiver is rarely used because the triggering mechanism did not work correctly. Later in its operation, the TDSS receiver was set to trigger off of the TDSF receiver (P.J. Kellogg, Personal Communication, 2010). This can result in a failure to observe large amplitude wave modes. On occasion, the TDSS receiver does return large amplitude wave modes which are of interest because they are often below the low frequency cutoff of TDSF (see Figures 10 through 12).

2.1.1 Langmuir Waves

Langmuir waves have been studied extensively in the terrestrial foreshock and somewhat at IP shocks [*Bale et al.*, 1997; *Fitzenreiter et al.*, 2003; *Kellogg et al.*, 1999]. Langmuir waves are usually linearly polarized parallel to the ambient magnetic field with narrow frequency peaks near f_{pe} . They are capable of pitch-angle scattering electrons and perturb the background density levels [*Soucek et al.*, 2005]. Langmuir waves are also thought to be the

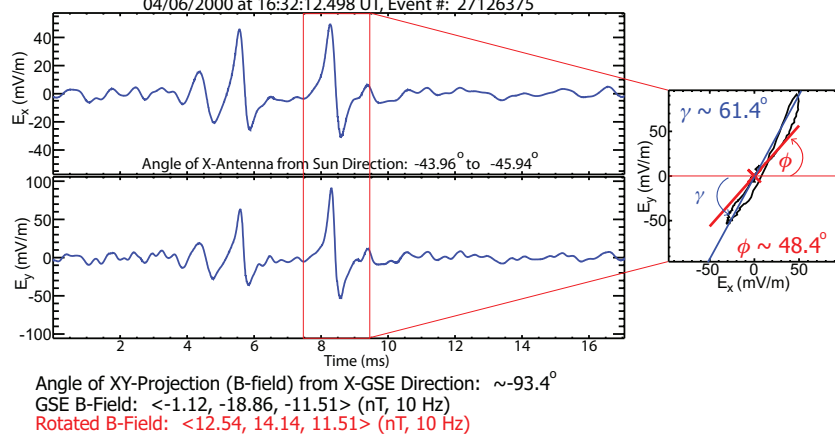


Figure 3: This is an example of a TDS sample from the Wind/WAVES instrument. The two panels on the left are the X and Y-antenna measurements of the electric field in the WAVES coordinate system. The hodogram on the right is a plot of E_x vs. E_y with the associated magnetic field rotated into the proper coordinate system. Notice the angle between the X-antenna and the sun-direction (θ from Figures 1 and 2) is roughly $-43.96^\circ \leq \theta \leq -45.94^\circ$ over the duration of the TDS sample. The angle of the XY-GSE projection of the magnetic field from the X-GSE direction is roughly -93.4° .

progenitors of solar radio emissions, specifically Type II and Type III radio bursts [Bale *et al.*, 1999; Kellogg, 2003; Pulupa and Bale, 2008; Pulupa *et al.*, 2010]. Though they are not directly related to collisionless shocks, the shock structure is related to the source of free energy for the Langmuir waves, electron beams [Kellogg, 2003]. Langmuir waves are also thought to scatter off of density perturbations, which can be a useful tool in describing source regions of radio bursts or shock structure [Krasnoselskikh *et al.*, 2007].

Figure 4 is an illustrative example of a linearly polarized Langmuir wave seen upstream of an IP shock on 04/06/2000 at 16:31:54.951 UT by the Wind spacecraft's TDS detector [Bougeret *et al.*, 1995]. The figure is a ~ 17 ms waveform capture that has been rotated into field-aligned coordinates defined by the XY-GSE projection of the magnetic field (due to only two component observations). The top two panels are the parallel (E_{\parallel} in red) and perpendicular (E_{\perp} in blue) projections of the electric field while the bottom two are the Morlet wavelet transforms. As one can see, Langmuir waves are high frequency (typically ~ 10 -50 kHz in the solar wind), linearly polarized, large amplitude (>10 mV/m) waves. They are

observed as both ES and electromagnetic in the solar wind [Bale *et al.*, 1999; Pulupa and Bale, 2008; Wilson III *et al.*, 2007].

Figure 4 is an example of a waveform capture of an electric field measurement of a Langmuir wave observed upstream of an IP shock. The electric fields have been rotated into field-aligned coordinates where the top panel (red electric field) is the parallel component, E_{\parallel} , and the second panel (blue electric field) is the perpendicular, E_{\perp} . In the top two panels are vertical black arrows that define the relative amplitudes of each component of the electric field measured. Below the two waveforms are the corresponding frequency spectrum calculated using wavelet analysis. To the right is a hodogram plotting E_{\perp} versus E_{\parallel} for the time range outlined by the magenta box in the top two panels to the left. The solid green line in the hodogram represents the XY-GSE projection of the shock normal vector in FACs. As one can see, this particular Langmuir wave appears to be linearly polarized roughly parallel to the magnetic field.

2.1.2 Ion-Acoustic Waves

A number of authors [Gurnett *et al.*, 1979a,b; Hess *et al.*, 1998; Thomsen *et al.*, 1985] have concluded that IAWs are important in dissipating energy in lower Mach number shocks. Wave amplitudes in previous studies were found to be correlated with the electron to ion temperature ratio, T_e/T_i [Gurnett *et al.*, 1979b]. They tend to be broadband bursty waves with Doppler shifted frequencies between 1-10 kHz (typically $f_{pi} < f < f_{pe}$) in the solar wind with a maximum intensity around 3 kHz [Gurnett *et al.*, 1979a,b; Hess *et al.*, 1998]. They are usually linearly polarized close to parallel or oblique to the ambient magnetic field [Akimoto *et al.* [1985]; Akimoto and Winske [1985]; Fuselier and Gurnett [1984]]. In a shock, the instability is thought to be driven by a relative drift between electrons and ions [Mellott, 1985], with threshold drifts increasing for small T_e/T_i . A number of studies have concluded that IAWs are likely to be dominant in the terrestrial bow shock despite questions about high damping effects due to small T_e/T_i [Akimoto *et al.*, 1985; Akimoto and Winske, 1985; Fuselier and Gurnett, 1984]. Theoretical studies suggest temperature gradients and oblique propagation of the waves can reduce damping when $T_e \sim T_i$.

Figure 5 is an example of an IAW observed in the shock ramp of an IP shock on 1996-04-08. The format is the same as Figure 4. As one can see, the wave appears to be roughly linearly polarized parallel to the magnetic field in the plane of measurement, though

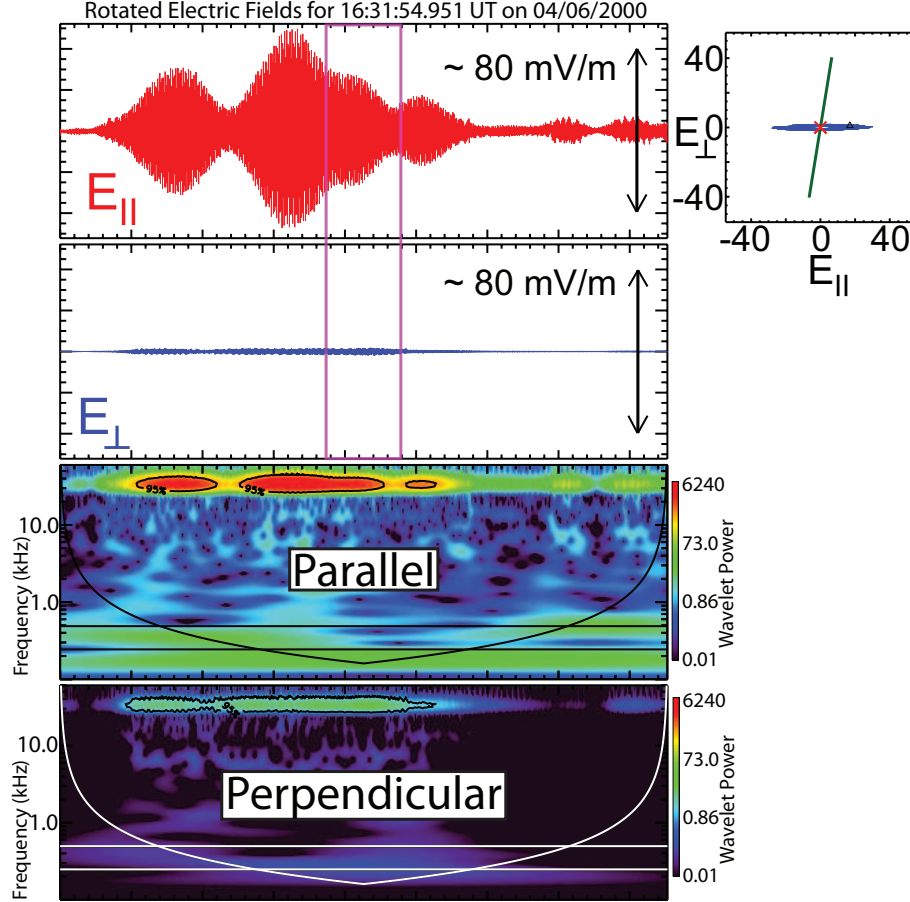


Figure 4: An example Langmuir wave observed upstream of the shock ramp of the 04/06/2000 event of *Wilson III et al.* [2009]. The top two panels are the parallel ($E_{||}$ in red) and perpendicular (E_{\perp} in blue) projections of the electric field while the bottom two are the Morlet wavelet transforms. The wavelets are plotted from 100 Hz to 60 kHz. The hodogram to the right plots E_{\perp} versus $E_{||}$ in the region outlined by the magenta box with the solid green line representing XY-GSE projection of the shock normal vector in FACs.

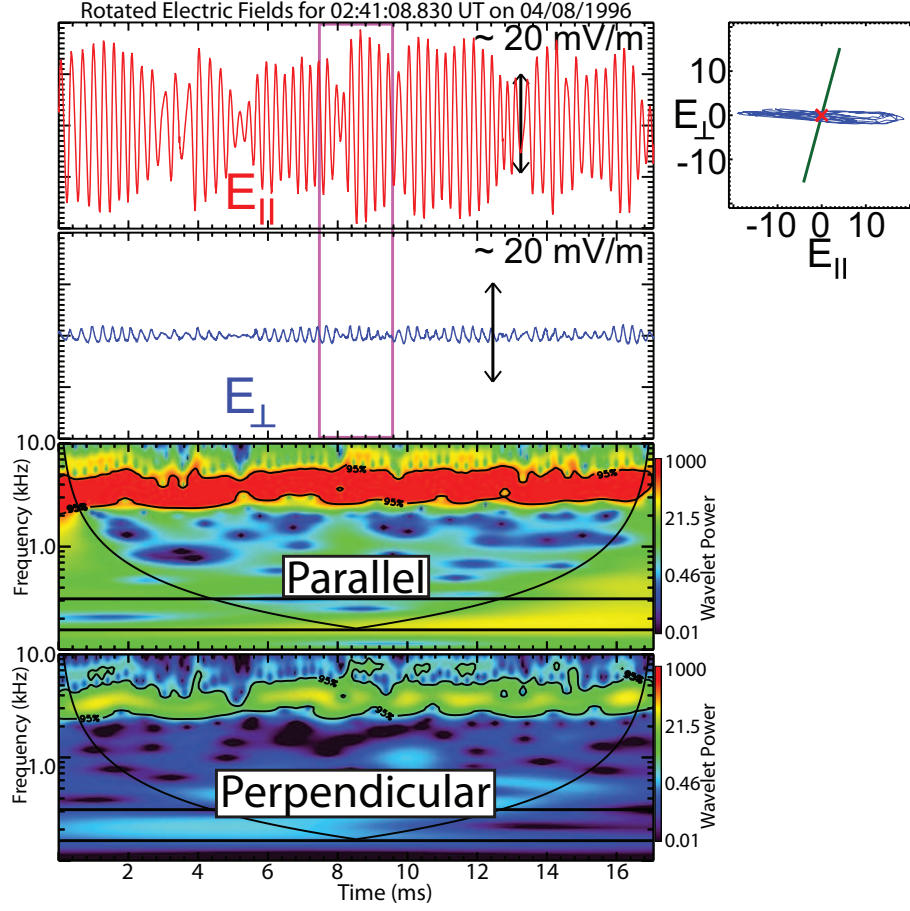


Figure 5: An example IAW observed in the shock ramp of the 04/08/1996 event of *Wilson III et al.* [2009]. The format is similar to that of Figure 4, except the wavelets are plotted from 100 Hz to 10 kHz.

their polarization can occasionally be quite oblique and more elliptical. They often exhibit a relatively narrow and well defined frequency peak, as illustrated in the wavelet transform plots below the waveforms.

2.1.3 Electrostatic Solitary Waves

ES solitary waves (ESWs) are characterized as nonlinear ES Debye-scale bipolar electric field signatures parallel to the ambient magnetic field [Cattell *et al.*, 2002a,b, 2005; Ergun *et al.*, 1998a; Franz *et al.*, 2005; Pickett *et al.*, 2004], often associated with electron beams [Cattell *et al.*, 2005; Ergun *et al.*, 1998a; Franz *et al.*, 2005]. Phase space holes were first thought to be a nonlinear mode consistent with a BGK mode by [Matsumoto *et al.*, 1994]. Thus, the component of the electric field parallel to the magnetic field is seen as a bipolar pulse while the components perpendicular are monopolar, both are derivatives of a Gaussian. Solitary waves have been observed at the Earth's bow shock [Bale *et al.*, 1998, 2002], and at an IP shock near ~ 8.7 AU [Williams *et al.*, 2005], as well as within the magnetosphere at many boundaries [Cattell *et al.*, 2002a,b, 2005] possibly providing energy dissipation. Simulations have shown them to form in and around the ramp regions of high Mach number collisionless shock waves [Matsukiyo and Scholer, 2006; Shimada and Hoshino, 2000].

ESWs act like clumps of positive charge, if electron holes. In the frame of the electron hole, the ions can be incident on the hole at very large speeds relative to their thermal speed. The relative speed is large because electron holes travel at roughly the electron drift velocity or fractions of electron beam speeds which is much much larger than the ion thermal speed [Behlke *et al.*, 2004; Cattell *et al.*, 2002a, 2003, 2005; Ergun *et al.*, 1998b,a; Franz *et al.*, 1998]. Since the structures are on the order of an electron Debye length, λ_{De} , the transit times of incident ions will be relatively small compared to the local ion gyroperiod. Thus, the ions can become demagnetized if scattered. To visualize this, assume an ion is incident on an electron hole with an impact parameter of b . Then the perpendicular impulse of the ion in response to the electron hole's electric field can be shown as:

$$M_i \Delta V_{i,\perp}(b) = e \int_{-\infty}^{\infty} dt E_{\perp}[b, z(t)] \quad (1)$$

where M_i is the ion mass, $\Delta V_{i,\perp}$ is the change in ion velocity, E_{\perp} is the electric field perpendicular to the magnetic field, and $z(t)$ is the position along the direction parallel to the

magnetic field at time t . If we assume that the incident ion velocity in the electron hole frame is V_{hole} and that the electron hole will not recoil upon impacting a single ion, then we can also estimate the parallel impulse of the ions as $\Delta V_{i,\parallel} \simeq -\Delta V_{i,\perp}^2 / (2 V_{hole})$. The net result is an exchange of momentum between the ions and the electrons both parallel and perpendicular to the magnetic field. If there is a relative drift between the two species, this momentum exchange can act to reduce the relative drift, thus reduce a current. In this way, electron holes can be effective waves for inducing anomalous resistivity. The end result is strong perpendicular ion heating (i.e. random perpendicular ion acceleration) and a significant amount of parallel momentum imparted upon the electrons from the ions. Observations have shown that $\Delta T_{i,\perp}$ across a train of electron holes can be a significant fraction of the ion thermal energy [Ergun *et al.*, 1998a].

Since the holes act like clumps of positive charge, they have positive potentials and thus act to trap incident electrons [Dyrud and Oppenheim, 2006; Lu *et al.*, 2008]. The particles that are trapped are the ones with energies below that of the max potential of the solitary structure. The accumulation of electrons trapped in the solitary structure acts to damp/saturate the instability driving the holes [Lu *et al.*, 2008]. In addition to trapping electrons, the electron holes can create double-peaked electron distributions at low energies which are unstable to other wave modes [Berthomier *et al.*, 2008; Matsukiyo and Scholer, 2006].

The last, somewhat indirect, way in which solitary waves can heat/scatter particles is by coupling to other wave modes. Solitary waves can either couple to or directly cause IAWs [Dyrud and Oppenheim, 2006], whistler mode waves [Lu *et al.*, 2008], and electron acoustic waves [Matsukiyo and Scholer, 2006]. IAWs are known to heat electrons parallel to their fluctuating electric fields (typically along the magnetic field) [Dum *et al.*, 1974]. Whistler waves are known to cause a perpendicular pitch-angle diffusion and heating of electrons [Brice, 1964; Kennel and Petscheck, 1966]. Electron acoustic waves are thought to produce strong parallel (with respect to the magnetic field) electron heating [Matsukiyo and Scholer, 2006], but to the best of our knowledge, these modes have not been observed.

Figure 6 is an example of an ESW observed by the Wind spacecraft in the terrestrial magnetosphere. The format is the same as Figures 4 and 5. Though these wave modes are observed at collisionless shocks, they are typically much larger amplitude in the magnetosphere making the characteristic bipolar signature more obvious. Notice that the defining characteristic, parallel component (red) is bipolar while the perpendicular is monopolar (blue), is very obvious in this example.

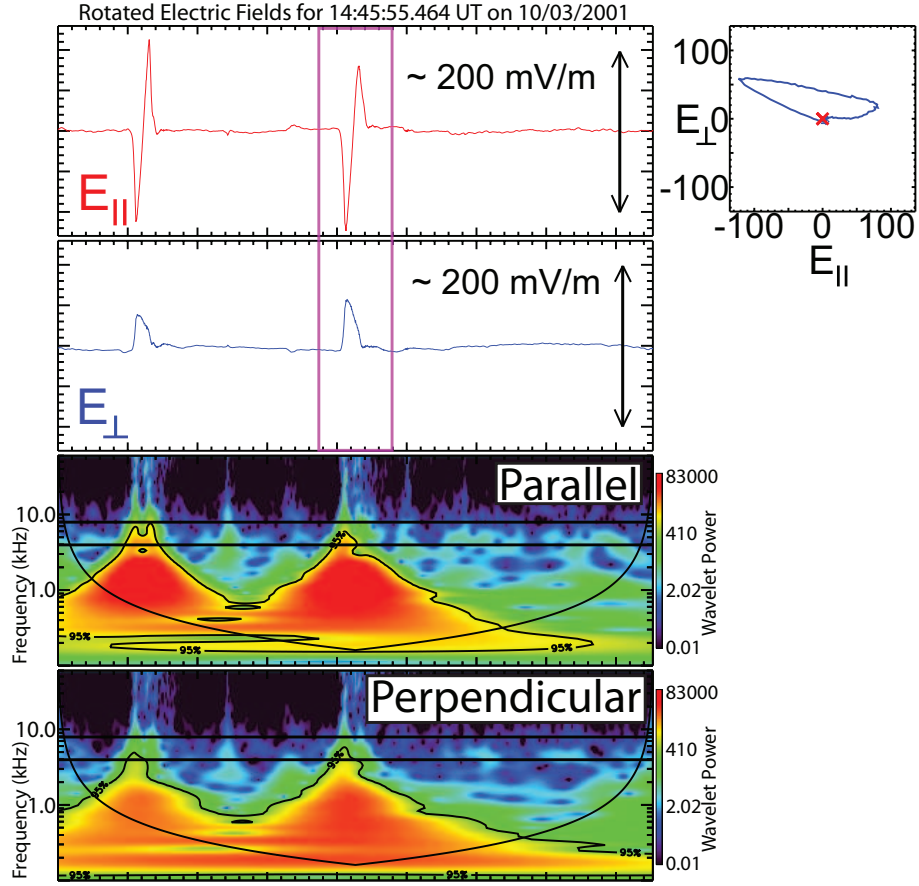


Figure 6: An example solitary wave observed in the terrestrial magnetosphere. The format is similar to that of Figures 4 and 5. The parallel and perpendicular component wavelet transforms are labeled respectively.

2.1.4 Whistler Waves

Whistler waves were first discovered by *Barkhausen* [1919] while listening to signals from an antenna connected to a simple vacuum tube amplifier. The signals were heard to decrease in frequency with increasing time. Over thirty years later, *Storey* [1953] managed to explain these strange signals as being the result of lightning strikes. It is now known that whistler waves can exist as a RH electromagnetic mode [*Kennel and Petscheck*, 1966] or a slightly electrostatic mode and interact with both ions [*Hoppe et al.*, 1982; *Stasiewicz et al.*, 2003] or electrons [*Brice*, 1964], [*Kennel and Petscheck*, 1966], and [*Lyons et al.*, 1972]. Due to their capacity to resonantly and nonresonantly interact with particles, whistler waves are a topic of extreme interest in collisionless shock dissipation topics.

A specific class of whistler wave is often observed immediately upstream of a quasi-perpendicular collisionless shock wave in magnetic field data, called precursor whistler waves or just precursor waves. Their existence was theorized as a necessary part of the shock structure since collisionless shock waves were first predicted [*Kellogg*, 1962]. The necessity of their existence at low Mach number collisionless shock waves was more rigorously shown by *Morton* [1964] and *Stringer* [1963]. These waves are low enough frequency that they couple to the magnetosonic wave responsible for the shock ramp. Thus, they can provide energy dissipation in shock waves through dispersive effects and wave-particle interactions upstream of the shock ramp [*Gary and Mellott*, 1985]. Occasionally precursor whistlers phase stand with respect to the shock front [*Fairfield and Feldman*, 1975], which means their phase velocity matches the shock front phase velocity. Therefore, in the shock frame of reference, the waves appear as standing wave modes. This condition is satisfied at the bow shock when the phase speed of the precursor whistler matches the shock wave phase speed and the group velocity exceeds the incident solar wind speed [*Greenstadt et al.*, 1975].

Figure 7 shows an example of a quasi-perpendicular, low Mach number IP shock with a precursor whistler wave (highlighted by purple box). The top panel shows the magnetic field magnitude and the bottom panel shows the three GSE components of the magnetic field. The fluctuations in the magnitude of the magnetic field illustrate the compressive and oblique nature of this class of whistler wave. This particular whistler was observed to propagate at an oblique angle to the magnetic field and has spatially dispersive properties.

Fairfield and Feldman [1975] initially identified precursor whistler waves at the quasi-perpendicular bow shock using magnetometer data from Explorer 43 as phase standing. Later studies, using OGO 5 [*Greenstadt et al.*, 1975] and ISEE 1 and 2

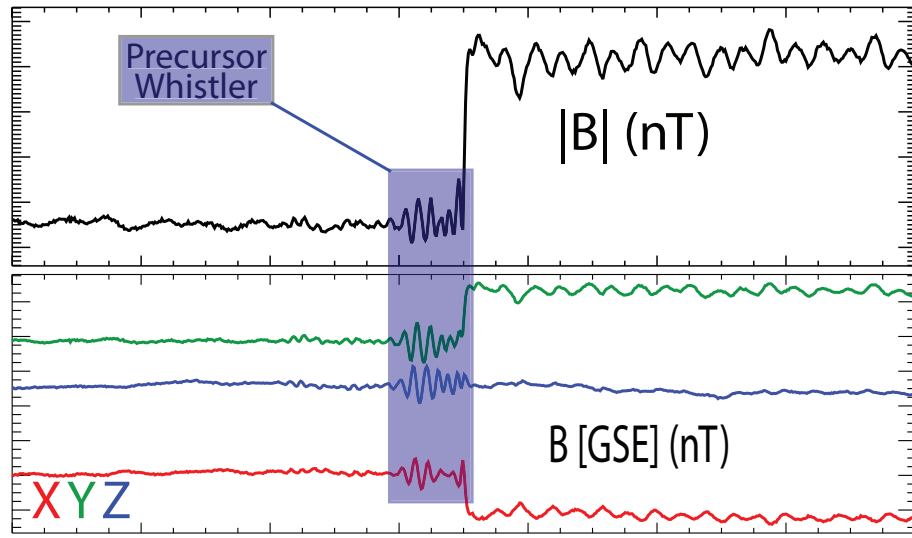


Figure 7: An example of an IP shock with an upstream precursor whistler wave. The top panel is the magnitude of the magnetic field and the bottom panel is the GSE components. The region with the precursor is outlined by the translucent blue box.

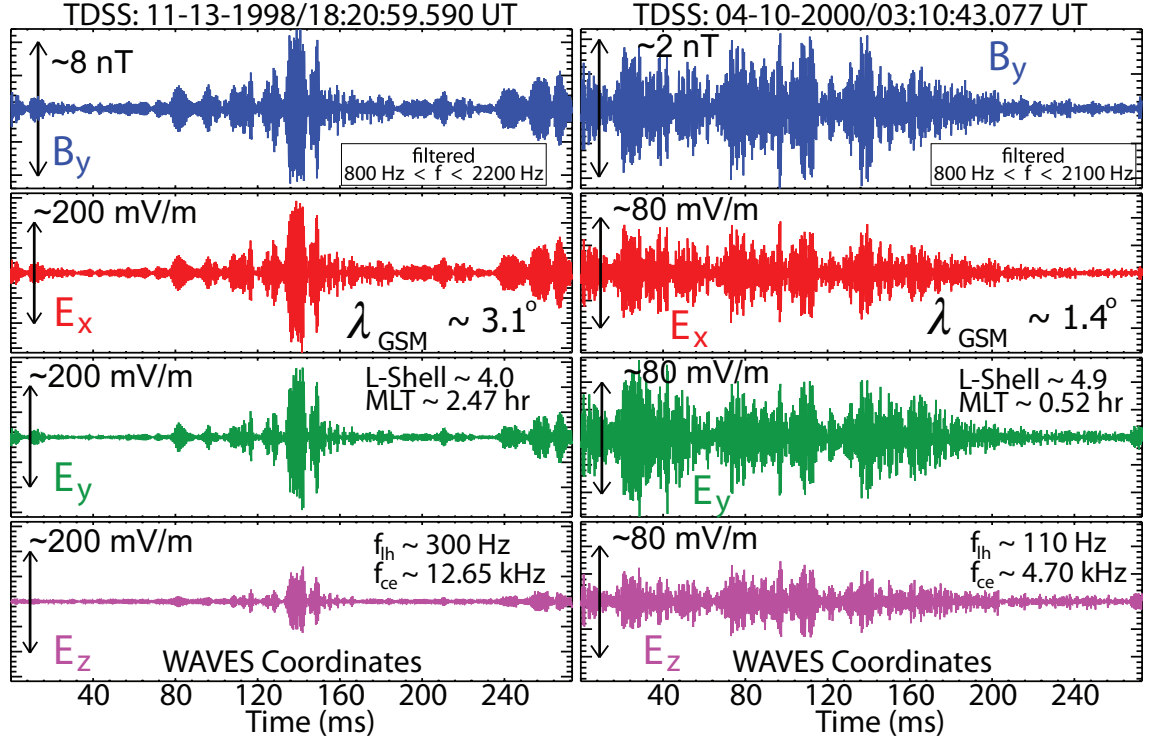


Figure 8: Examples of two whistler waves, in instrument coordinates, observed on the perigee passes of Wind on 1998-11-13 and 2000-04-10. The examples were taken from the TDSS instrument and filtered (frequency range shown in top panels) to remove superposed low and high frequency signals. The top row shows the Y-component of the magnetic field (blue), second row shows the X-component of the electric field (red), third row shows the Y-component of the electric field (green), and the fourth row shows the Z-component of the electric field (magenta). The amplitudes of each component are marked by the vertical black arrows. The TDSS samples for these two events were taken at 7.5 kHz.

[*Mellott and Greenstadt*, 1984] magnetometer data, found many of the upstream waves to be inconsistent with phase standing whistlers. *Mellott and Greenstadt* [1984] found two different types of precursor whistler waves, a phase standing whistler wave propagating parallel to the shock normal and another whistler propagating parallel to the magnetic field. In the SC frame, the precursors propagating parallel to the magnetic field had higher frequencies (~ 1 Hz) than the phase standing precursor whistlers (~ 0.1 Hz). It is important to note that the ~ 1 Hz waves studied by *Hoppe et al.* [1982] had relatively large θ_{kB} values, while the precursors of *Mellott and Greenstadt* [1984] were propagating parallel to the magnetic field, thus $\theta_{kB} \sim 0^\circ$. *Mellott and Greenstadt* [1984] proposed that the parallel propagating precursors were products of the phase standing precursors. The precursors propagating parallel to the shock normal (the phase standing precursors) were found to have higher rest frame frequencies than the precursors propagating parallel to the magnetic field. The difference was due to their propagation with respect to the magnetic field. The Doppler effects on the parallel propagating precursors were negligible because the magnetic field was primarily directed in Y-GSE direction, roughly perpendicular to the solar wind velocity. Both the parallel propagating and phase standing precursors are characterized by a high degree of RH polarization and nearly monochromatic frequency spectrum. A more recent study by *Farris et al.* [1993] found that the comparison between observed and predicted wavelengths for phase standing precursor whistlers to be consistent with the results of *Mellott and Greenstadt* [1984]. However, the estimates by *Farris et al.* [1993] of the ratio of precursor whistler wavelength to shock thickness differed from those of *Mellott and Greenstadt* [1984]. Thus, *Farris et al.* [1993] concluded that the thickness of the shock ramp was not strictly dependent/related to the wavelength of the precursor whistler.

The following is taken from *Wilson III et al.* [2010a]:

Figure 8 plots two whistler waves observed near the equatorial plane, post midnight near $L \sim 4$. These whistlers were obtained from the TDSS instrument (with three electric and one magnetic field sampled at 7.5 kHz); the waveforms shown were filtered (frequency range shown in top panels) to remove superposed low and high frequency signals. The L-shell, MLT, GSM latitude, lower hybrid frequency ($f_{lh} = \sqrt{f_{ce}f_{ci}}$), and f_{ce} for each corresponding whistler are labeled in the figure. Note that the 8 nT peak-to-peak amplitude we report here is only one component of the magnetic field. The total magnetic amplitude for both waveforms shown in Figure 8 is larger. The polarization of the electric fields is elliptical for both examples. The 1998-11-13 example is much more oblique ($\theta_{kB} \sim 73^\circ$) and elliptical ($\lambda_{max}/\lambda_{min} \sim 10.7$) than the 2000-04-10 example ($\theta_{kB} \sim 39^\circ$ and $\lambda_{max}/\lambda_{min} \sim 1.9$). *Omura*

et al. [2007] gave a relationship for the maximum change in kinetic energy given by:

$$(\Delta KE)_{max} \approx \frac{5.6 \times 10^4}{L^2 \sqrt{1 + \xi_o^2}} \frac{\delta B}{B_o} [MeV] \quad (2)$$

where L is the L-shell, $\xi_o^2 = \omega (\Omega_{EQ} - \omega) / \omega_{pe}^2$, Ω_{EQ} is the equatorial cyclotron frequency, and $\delta B/B_o$ is the ratio of wave amplitude to background magnetic field. For the waves shown in Figure 8, $(\Delta KE)_{max} \sim 61$ MeV (28 MeV) for the wave on 1998-11-13 (2000-04-10). The examples show that: (1) large amplitude whistler waves in the radiation belts are bursty; (2) electric fields are in excess of two orders of magnitude above previous estimates; (3) the first observations of these very large amplitude whistler waves with search coil magnetic fields shows amplitudes exceeding two orders of magnitude above previous estimates; and (4) the waves are capable of producing electrons with energies greater a MeV.

Since we only have four field components for each TDSS sample, we cannot fully describe the wave Poynting flux. However, we can calculate part of two components to estimate the magnitude of the Poynting flux for these waves. The 1998-11-13 (2000-04-10) whistler in Figure 8 has Poynting flux magnitude of $\gtrsim 300 \mu W/m^2$ ($\gtrsim 30 \mu W/m^2$), which is roughly four (three) orders of magnitude larger than the estimates found by *Santolík et al.* [2010]. To estimate the possible impact of the large Poynting fluxes, we perform the calculation of *Santolík et al.* [2010] assuming the same estimates of $\gtrsim 1$ MeV electron fluxes, background densities, and field-aligned column area (of a flux tube). We find that it would take roughly 5 ms (50 ms) for the whistlers seen in Figure 8 to deposit the necessary energy density ($\sim 10^{-4}$ J/m²) to accelerate plasma sheet electrons to 1 MeV, assuming 100% efficiency, in the outer radiation belt. If we now assume a 1% efficiency, we find a time scale of 0.5 seconds (5.5 seconds) necessary for these whistlers to produce the same effect. These estimates are five to six orders of magnitude shorter than the typical estimates. However, as one can see in Figure 8, these whistlers are very bursty and their amplitudes are not sustained for longer than 10's of milliseconds. We should also note that the larger amplitude waves we observe will likely not interact with electrons in the same quasi-linear fashion as described by *Santolík et al.* [2010].

2.1.5 Waves at or Near the Electron Cyclotron Frequency

Electron cyclotron harmonic, electron Bernstein, $(n + 1/2)$, or "totem pole" waves have been observed throughout planetary magnetospheres by *Barbosa et al.* [1990] and *Usui*

et al. [1999]. These emissions can be both broad or narrow in frequency range [Hubbard and Birmingham, 1978]. They are typically driven unstable by loss-cone or anisotropic electron distributions in the high energy hot halo in planetary magnetospheres. Usui *et al.* [1999], in a study near the terrestrial magnetopause, found the emissions to be associated with increases in the ratio of hot halo to cold core electron densities, n_h/n_c . To the best of our knowledge, these emissions have not been observed previously in the solar wind.

Figure 9 shows two examples of electron cyclotron harmonic waves observed downstream of an IP shock by the Wind spacecraft. The top(bottom) four panels correspond to the waveform observed at 16:32:25.358 UT(16:32:25.428 UT) on 04/06/2000. These waves were observed downstream of the interplanetary shock studied in detail by Wilson III *et al.* [2010b]. The top row of panels for each waveform with the red(blue) lines correspond to the $E_{\parallel}(E_{\perp})$ component of the wave electric field. The bottom two panels of each waveform show the power spectra ($\text{mV}/\text{m}^2/\text{Hz}$) versus frequency (kHz) plots corresponding to the time range defined by the orange box in the top two panels. The vertical green(magenta) lines overplotted on the power spectra correspond to integer(half-integer) harmonics of f_{ce} . Note that the 16:32:25.358 UT waveform primarily shows enhanced power at integer harmonics of f_{ce} while the 16:32:25.428 UT waveform shows mixtures of integer and half-integer harmonics of f_{ce} . The wave power enhancements shift dynamically in time throughout the waveform, thus why only small windows of time were used to calculate the power spectra. These waveforms are over two orders of magnitude above the background levels ($\sim 0.1 \text{ mV}/\text{m}$ at 1 AU).

Simulations have found bipolar ES phase space holes form in and around the ramp regions of high Mach number collisionless shock waves [Dyrud and Oppenheim, 2006; Matsukiyo and Scholer, 2006]. Due to their ability to efficiently exchange momentum between electrons and ions, the holes can heat and scatter particles. Simulations also show that the holes can also couple with other wave modes like IAWs and lower hybrid waves, providing resistive dissipation [Dyrud and Oppenheim, 2006; Matsukiyo and Scholer, 2006]. Matsukiyo and Scholer [2006] examined microinstabilities in the foot of supercritical collisionless shocks using a two dimensional PIC simulation with a realistic mass ratio ($M_i/m_e \sim 1836$). They observed six different types of instabilities excited in less than an ion gyroperiod with the dominant modes including EC DI, whistler instability, electron acoustic instability, and two different modified two-stream instabilities (MTSIs); MTSI-2 excited by relative drifts between incident electrons and reflected ions and MTSI-1 due to the relative drift between electrons and incident ions. Reflected ions cause the incident solar wind ions to decelerate

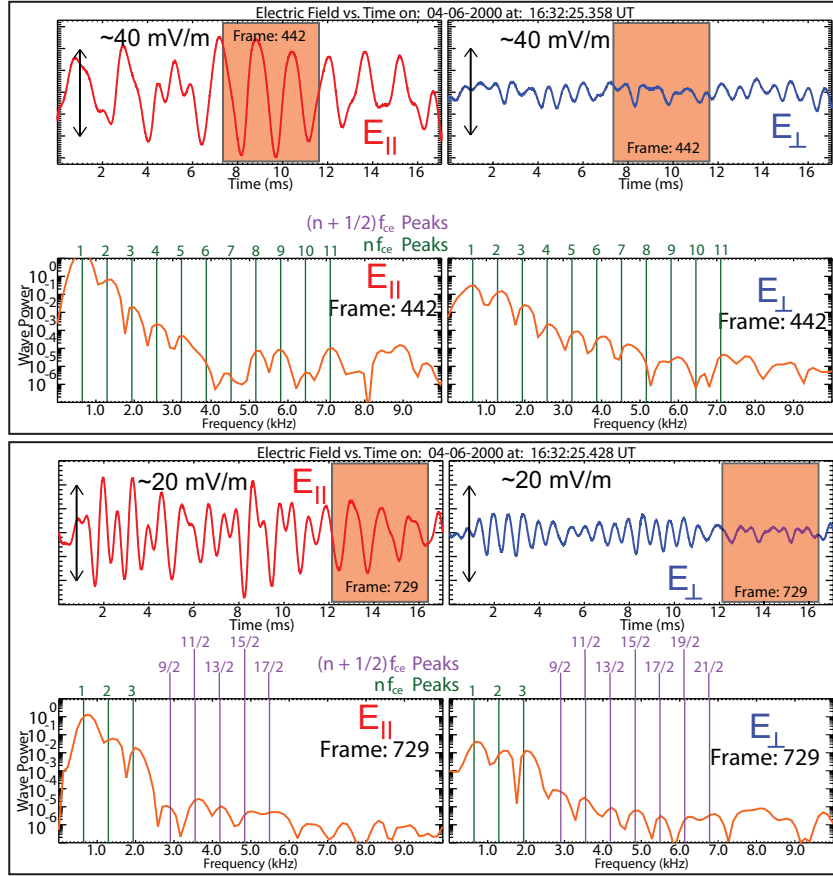


Figure 9: Two examples of electron cyclotron harmonic waves observed downstream of an IP shock. The top waveform was observed at 16:32:25.358 UT and the bottom at 16:32:25.428 UT. The top row contains E_{\parallel} (red) and E_{\perp} (blue). Below the waveforms are the power spectra (mV/m²/Hz) versus frequency (kHz) plots corresponding to the time range defined by the orange box. The vertical green(magenta) lines overlotted on the power spectra correspond to integer(half-integer) harmonics of f_{ce} . The 16:32:25.428 UT has a similar format.

in the shock foot, which locally decelerate the electrons to maintain current continuity in the shock normal direction. These instabilities give rise to waves which scatter and heat the plasma, thus dissipating energy.

2.1.6 Lower Hybrid Waves

Lower hybrid waves (LHWs) are typically an electrostatic (ES) mode propagating perpendicular to the magnetic field with a frequency given by:

$$f_{lh}^2 = \frac{f_{ce}f_{ci}}{1 + (f_{ce}f_{ci})/f_{pi}^2} \quad (3)$$

where f_{cs} is the cyclotron frequency of species s and f_{pi} is the ion plasma frequency. In the high density limit ($f_{pi}^2 \gg f_{ce}f_{ci}$), typical of the solar wind, $f_{lh} \sim (f_{ce}f_{ci})^{1/2}$. LHWs are capable of resonating with the bulk of the ion distribution, thus they can serve as an effective ion heating mechanism [Davidson and Gladd, 1975; Lemons and Gary, 1978; Mellott, 1985]. In the ES limit and large propagation angles, the waves can couple the parallel motion of the electrons to the perpendicular motion of the ions [Marsch and Chang, 1983]. LHWs can be driven unstable by cross-field currents [Lemons and Gary, 1978], electron heat flux in the solar wind [Marsch and Chang, 1982], and the lower-hybrid drift instability (LHDI) [Cairns and McMillan, 2005]. They are an attractive candidate for resistive energy dissipation in collisionless shocks because their critical drift speeds, $V_{dcr} \approx V_{Ti}$, are much lower than that of an IAW, $V_{dcr} \approx V_{Te}$. LHWs can couple to other wave modes like drift waves, modified two-stream instabilities (MTSIs), etc., all of which cause significant wave-particle interactions [Lemons and Gary, 1978]. LHWs can heat the ions transverse to the magnetic field producing anisotropic ion distributions [Marsch and Chang, 1982]. Because LHWs have $\omega/k_{\parallel} \gg \omega/k_{\perp}$, they tend to interact with the higher energy electrons producing broadened high energy tails [Cairns and McMillan, 2005].

Electromagnetic lower hybrid waves (EMLHWs), or hybrid whistler waves, propagate nearly perpendicular to the ambient magnetic field and can appear to have a broadband frequency spectrum. One should note that in the limit of large k_{\perp} , LHWs are on the same branch of the dispersion relation as whistler waves. As with the ES LHWs, they are thought to be driven unstable by the solar wind electron heat flux [Marsch and Chang, 1983]. They can, much like ES LHWs, heat the ions perpendicular to the magnetic field. For these modes, $V_{i,res,\perp} \approx \omega/k_{\perp} \ll \omega/k_{\parallel} \approx V_{e,res,\parallel}$, which means the Landau interactions are perpendicular

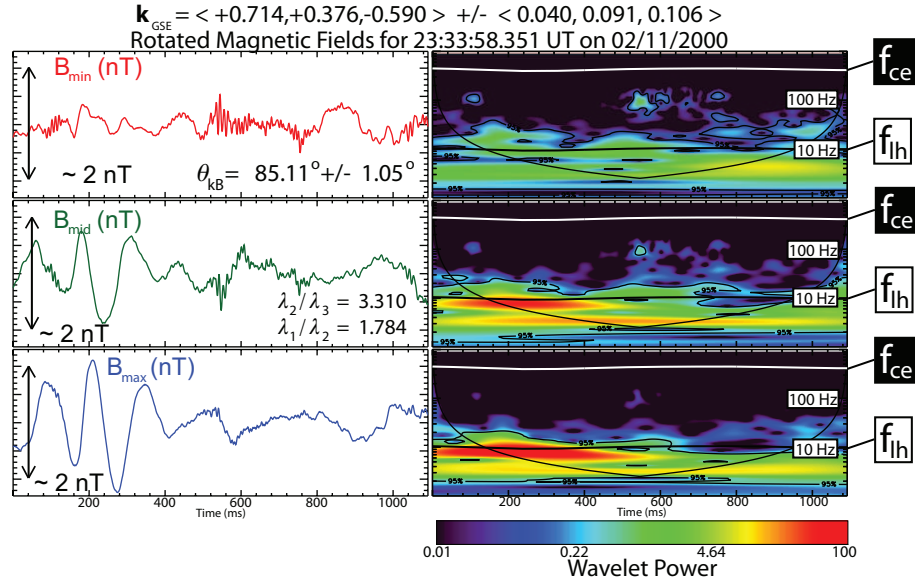


Figure 10: An example TDSS sample observed downstream of the shock ramp of an IP shock observed by the Wind spacecraft on 02/11/2000. The left-hand side of the plot shows the three components of the magnetic field measured by the TDSS detector search coils on Wind in minimum variance coordinates. The right-hand side of the plot shows the corresponding wavelet transforms. To the right of the wavelets are the labels of the relevant frequencies for this wave, where f_{ce} is the electron cyclotron frequency and f_{lh} is the lower hybrid resonance frequency. Other relevant information is given in the plot including the wave vector, \mathbf{k} , in GSE coordinates, the angle of propagation with respect to the magnetic field, θ_{kB} , and the eigenvalue ratios, λ_1/λ_2 and λ_2/λ_3 .

for the ions and parallel for the electrons, with respect to the magnetic field. They have frequencies of $f_{ci} \ll f \ll f_{ce}$ [Marsch and Chang, 1983]. These waves dissipate their wave energy through Landau interaction with the ions producing perpendicular ion heating. They propagate very obliquely to the field within a cone defined by $k_{\parallel}/k_{\perp} \leq 1/5$ and $k_{\parallel}/k_{\perp} \geq V_{Ti,\perp}/V_{Te,\parallel}$ [Marsch and Chang, 1983]. Zhang and Matsumoto [1998] observed EMLHWs at an IP shock using Geotail and showed that the waves propagate nearly perpendicular to the magnetic field.

Another related wave mode is the LHDI, which in the presence of strong plasma gradients, acts like a fluid instability excited through the coupling of a LHW and a drift wave [Davidson and Gladd, 1975; Huba *et al.*, 1978]. When the gradients are weak, the LHDI is a kinetic instability driven by a resonance between ions and a drift wave. When in the presence of a finite plasma β , the LHDI exists as an ES and electromagnetic mode [Davidson and Gladd, 1975; Huba *et al.*, 1978]. The growth rate of the LHDI peaks at $k\rho_e \approx 1$, for a broad range of frequencies near f_{lh} [Davidson and Gladd, 1975; Cairns and McMillan, 2005]. The mode is strongly unstable when the magnetic field gradient scale length, L_B , is comparable to ρ_i . The LHDI produces strong anomalous resistivity due to the wave's electric fields, $\delta\mathbf{E}_{\perp}$, perpendicular to the ambient magnetic field, \mathbf{B}_o , which create $(\delta\mathbf{E}_{\perp} \times \mathbf{B}_o)$ -drifts that transport particles across \mathbf{B}_o . Thus, the LHDI causes cross-field diffusion which is an increase in entropy, thus irreversible and important for energy dissipation [Coroniti, 1985].

Figure 10 is a TDSS sample observed downstream of the shock ramp of an IP shock observed by the Wind spacecraft on 02/11/2000. The waveform is an example of an EMLHW. The left-hand side of the plot shows the three components of the magnetic field measured by the TDSS detector search coils on Wind in minimum variance coordinates. The right-hand side of the plot shows the corresponding wavelet transforms. To the right of the wavelets are the labels of the relevant frequencies for this wave, where f_{ce} is the electron cyclotron frequency and f_{lh} is the lower hybrid resonance frequency. In the left-hand panel, one can see the angle of propagation with respect to the magnetic field is $\theta_{kB} \sim 85^\circ$, roughly perpendicular to the magnetic field. Note that at multiple points in the waveform, there appear to be low and high frequency signals intermixed. At roughly 400 ms, a higher frequency (at roughly 100 Hz), is superposed on the lower frequency (~ 10 Hz or $\sim f_{lh}$) signal.

Figure 11 shows the result of filtering the signal for $7 \text{ Hz} < f < 20 \text{ Hz}$ for discussion of frequency filtering). Note that the mid-to-min eigenvalue ratio, λ_2/λ_3 , is much higher now at ~ 12 compared to ~ 3 in Figure 10. Also, θ_{kB} has increased to $\sim 90^\circ$, consistent with previous observations [Zhang and Matsumoto, 1998] and theory [Marsch and Chang, 1983].

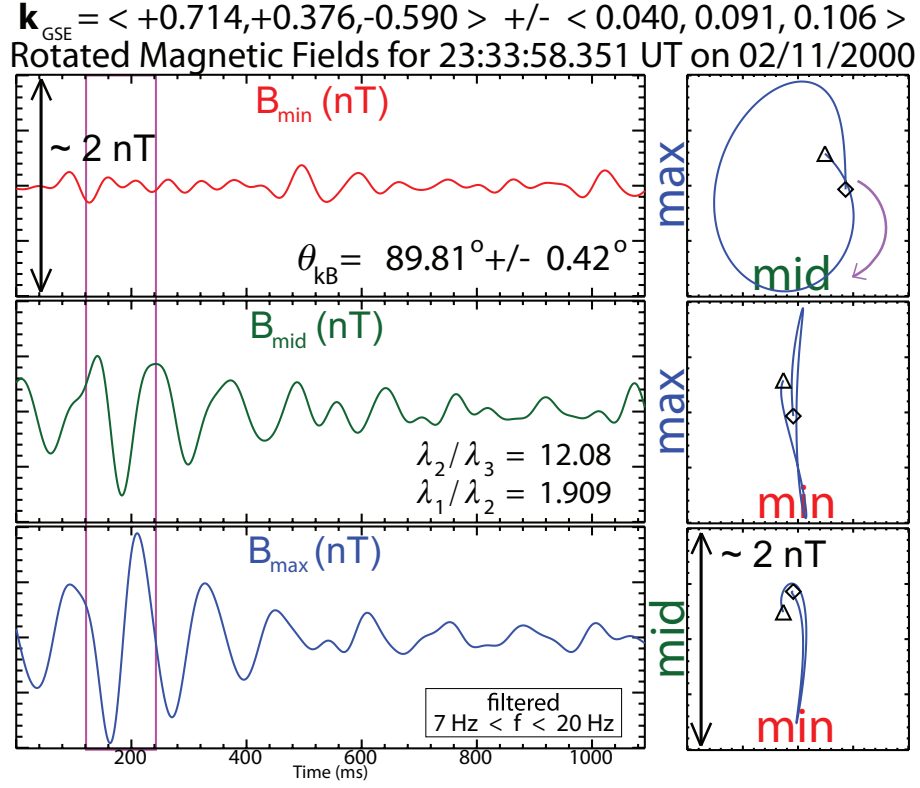


Figure 11: The low frequency filter ($7 \text{ Hz} < f < 20 \text{ Hz}$) of the TDSS sample observed downstream of the 02/11/2000 IP shock ramp in Figure 10. The left-hand side of the plot shows the three components of the magnetic field measured by the TDSS detector search coils on Wind in minimum variance coordinates. The right-hand side of the plot shows the corresponding hodograms.

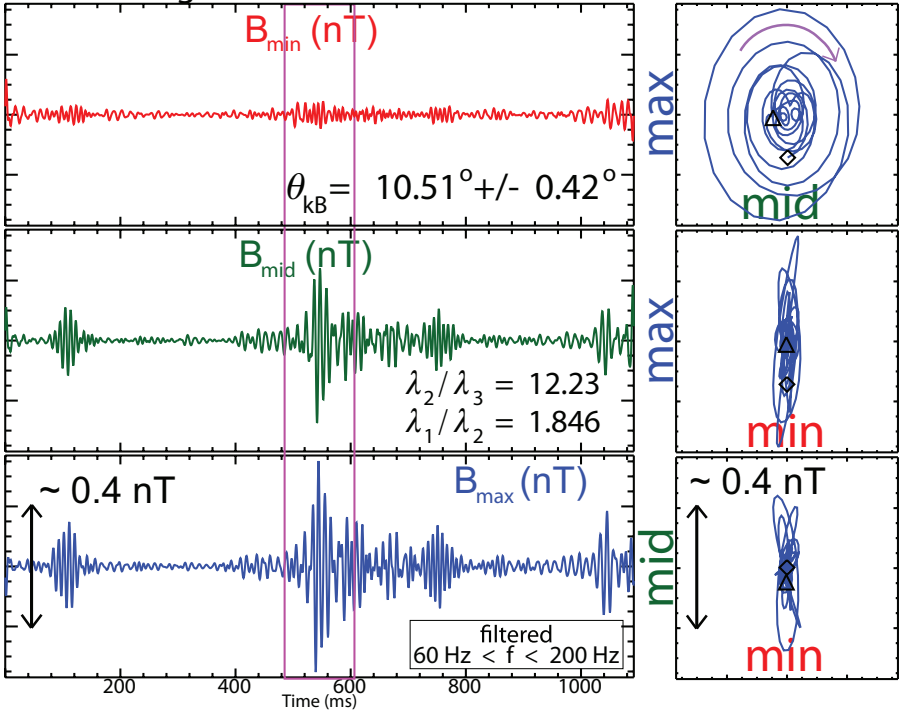
$$\mathbf{k}_{\text{GSE}} = \langle -0.585, +0.810, +0.045 \rangle \pm \langle 0.054, 0.039, 0.006 \rangle$$


Figure 12: The high frequency filter ($60 \text{ Hz} < f < 200 \text{ Hz}$) of the TDSS sample observed downstream of the 02/11/2000 IP shock ramp in Figure 10. The left-hand side of the plot shows the three components of the magnetic field measured by the TDSS detector search coils on Wind in minimum variance coordinates. The right-hand side of the plot shows the corresponding hodograms.

The amplitude of the low frequency component is ~ 1 nT.

Figure 12 shows the result of filtering the signal for $60 \text{ Hz} < f < 200 \text{ Hz}$. The format is the same as in Figure 11, but the amplitude of the wave is smaller and it is right-hand polarized with respect to the magnetic field, consistent with an electromagnetic whistler wave. The wave is propagating at a slightly oblique angle with respect to the magnetic field, which is roughly anti-parallel to the wave vector.

2.2 Magnetic Field Rotations

The magnetic field data is typically obtained in GSE coordinates and thus we need to rotate the data into WAVES coordinates, as explained in Section 2.1, for polarization analysis. Figure 3 shows an example of TDSF sample in 120 kHz sample rate. The event, shown in WAVES coordinates, is an example of a large amplitude solitary wave observed just downstream of an IP shock observed on 2000-04-06. On the left, the top(bottom) panel is a plot of $E_x(E_y)$. To the right is the hodogram, plot of E_x vs. E_y , for the region outlined by the red box in the left two panels. Overplotted on the hodogram, with a red line, is the XY-projection of the background DC magnetic field. The angle of the X-antenna from the sun direction varies from -43.96° to -45.94° over the course of the 17 ms TDS sample. In GSE coordinates, the XY-GSE projection of the DC magnetic field is roughly -93.4° away from the sun direction, thus varies away from the X-antenna by roughly 44.8° (shown in red in the hodogram). Notice that the bipolar signature of the solitary wave is roughly aligned with the magnetic field, consistent with magnetospheric observations [Ergun *et al.*, 1998b,a; Franz *et al.*, 2000].

2.2.1 Radio Receivers

The TNR measures ~ 4 -256 kHz electric fields in up to 5 logarithmically-spaced frequency bands, though typically only set at 3 bands (K. Goetz, Personal Communication, 2007), from 32 or 16 channels per band, with a $7 \text{ nV}/\sqrt{\text{Hz}}$ sensitivity, 400 Hz to 6.4 kHz bandwidth, and total dynamic range in excess of 100 dB [Bougeret *et al.*, 1995]. The data are taken by two multi-channel receivers which nominally sample for 20 ms at a 1 MHz sampling rate (see Table 2 for more information). The TNR is often used to determine the local plasma density by observing the plasma line, an emission at the local plasma frequency due to a thermal noise response of the wire dipole antenna. One should note that observation of the plasma line requires the dipole antenna to be longer than the local λ_{De} [Meyer-Vernet and Perche, 1989]. For typical conditions in the solar wind, the wire dipole antenna on Wind

easily satisfy this condition.

Table 2: Wind WAVES TNR Specs

Band	Range (kHz)	Sampling Rate (kHz)	Measurement Time (ms)
A	4-16	64.1	320
B	8-32	126.5	160
C	16-64	255.7	80
D	32-128	528.5	40
E	64-256	1000.0	20

3 SCET Corrections

The TDS samples are waveform captures of electric and magnetic field data. The data is triggered by the largest amplitude waves which exceed a specific threshold and are then stored in a memory buffer. The TDS datation time is sampled after the event is acquired which requires a delay buffer. The datation time requires two corrections. The first correction arises from tagging the TDS datation with an associated spacecraft major frame in house keeping (HK) data. The second correction removes the delay buffer duration. Both inaccuracies are essentially artifacts of on ground derived values in the archives created by the WINDlib software (K. Goetz, Personal Communication, 2008).

The WAVES instrument’s HK mode sends relevant low rate science back to ground once every spacecraft major frame. If multiple TDS events occur in the same major frame, it is possible for the WINDlib software to assign them the same SCETs. One can correct these issues to within +10 ms. This is often not necessary since the highest sampling rate of the HTR MFI data is only 22 Hz, however there are occasions where the 0.33 Hz data differs from the HTR data by $> 20^\circ$. As a consequence, the polarization analysis (see hodogram in Figure 3) can be misleading.

The TDS receiver onboard calculations force the peak amplitude of the data to occur roughly in the center of the waveform capture time window. Thus the data is sampled from both before and after the peak. The time stamps associated with the data sampled after the peak is easily obtained but the times before the peak require the delay buffer memory. The delay buffer duration depends on sampling rate and waveform duration. WINDlib attempts to fix the delay buffer uncertainty but it cannot correct the built-in timing error of ~ 300 ms when sampling at 120 kHz. One should note that for lower sample rates, the timing error

is larger (K. Goetz, Personal Communication, 2008).

The TDSF receiver (sampled at 120 kHz) time stamps retrieved from WINDlib, before corrections, are accurate to +300 ms. The 300 ms uncertainty, due to the HK corrections mentioned above, results from WINDlib trying to recreate the time stamp after it has been telemetered back to ground. If an event stays in the TDS buffer for extended periods of time (*i.e.* >2 days), the interpolation done by WINDlib can make mistakes in the 11th significant digit. The positive definite nature of this uncertainty is due to rounding errors associated with the onboard DPU clock rollover. The DPU clock is a 24 bit integer clock sampling at $\sim 50,018.8$ Hz. The clock rolls over at ~ 5366.691244092221 seconds¹ (K. Goetz, Personal Communication, 2008). The sample rate is a temperature sensitive issue and thus subject to change over time. From a sample of 384 different points on 14 different days, a statistical estimate of the rollover time is $5366.691124061162 \pm 0.000478370049$ seconds.

The method by which to correct the SCETs is as follows:

1. Retrieve the DPU clock times, SCETs, UR8 times, and DPU Major Frame Numbers from the Windlib libraries on the VAX/ALPHA systems for the TDSS(F) data of interest.
2. Retrieve the same quantities from the HK data.
3. Match the HK event with the same DPU Major Frame Number as the TDSS(F) event of interest.
4. Find the difference in DPU clock times between the TDSS(F) event of interest and the HK event with matching major frame number (Note: The TDSS(F) DPU clock time will always be greater than the HK DPU clock if they are the same DPU Major Frame Number and the DPU clock has not rolled over).
5. Convert the difference to a UR8 time and add this to the HK UR8 time. The new UR8 time is the corrected UR8 time to within +10 ms.
6. Find the difference between the new UR8 time and the UR8 time WINDlib associates with the TDSS(F) event. Add the difference to the DPU clock time assigned by WINDlib to get the corrected DPU clock time (Note: watch for the DPU clock rollover).

¹The calculation is done by $(16 \cdot 2^{24}) / (50,018.8 \text{ Hz})$

7. Convert the new UR8 time to a SCET using either the IDL Windlib libraries or TMLib libraries of available functions. This new SCET is accurate to within +10 ms.

References

- Akimoto, K., and D. Winske (1985), Ion-acoustic-like waves excited by the reflected ions at the earth's bow shock, *J. Geophys. Res.*, *90*, 12,095–+, doi:10.1029/JA090iA12p12095.
- Akimoto, K., K. Papadopoulos, and D. Winske (1985), Ion-acoustic instabilities driven by an ion velocity ring, *J. Plasma Phys.*, *34*, 467–479.
- Aptekar, R. L., et al. (1995), Konus-W Gamma-Ray Burst Experiment for the GGS Wind Spacecraft, *Space Science Reviews*, *71*, 265–272, doi:10.1007/BF00751332.
- Bale, S. D., D. Burgess, P. J. Kellogg, K. Goetz, and S. J. Monson (1997), On the amplitude of intense Langmuir waves in the terrestrial electron foreshock, *J. Geophys. Res.*, *102*, 11,281–11,286, doi:10.1029/97JA00938.
- Bale, S. D., P. J. Kellogg, D. E. Larson, R. P. Lin, K. Goetz, and R. P. Lepping (1998), Bipolar electrostatic structures in the shock transition region: Evidence of electron phase space holes, *Geophys. Res. Lett.*, *25*, 2929–2932, doi:10.1029/98GL02111.
- Bale, S. D., M. J. Reiner, J.-L. Bougeret, M. L. Kaiser, S. Krucker, D. E. Larson, and R. P. Lin (1999), The source region of an interplanetary type II radio burst, *Geophys. Res. Lett.*, *26*, 1573–1576, doi:10.1029/1999GL000293.
- Bale, S. D., A. Hull, D. E. Larson, R. P. Lin, L. Muschietti, P. J. Kellogg, K. Goetz, and S. J. Monson (2002), Electrostatic Turbulence and Debye-Scale Structures Associated with Electron Thermalization at Collisionless Shocks, *Astrophys. J.*, *575*, L25–L28, doi:10.1086/342609.
- Barbosa, D. D., W. S. Kurth, I. H. Cairns, D. A. Gurnett, and R. L. Poynter (1990), Electrostatic electron and ion cyclotron harmonic waves in Neptune's magnetosphere, *Geophys. Res. Lett.*, *17*, 1657–1660, doi:10.1029/GL017i010p01657.
- Barkhausen, H. (1919), Zwei mit Hilfe der neuen Verstärker entdeckte Erscheinungen, *Phys. Zeitschrift*, *20*, 401–403.
- Behlke, R., M. André, S. D. Bale, J. S. Pickett, C. A. Cattell, E. A. Lucek, and A. Balogh (2004), Solitary structures associated with short large-amplitude magnetic structures (SLAMS) upstream of the Earth's quasi-parallel bow shock, *Geophys. Res. Lett.*, *31*, 16,805–+, doi:10.1029/2004GL019524.
- Berthomier, M., G. Dubois, and L. Muschietti (2008), Stability of three-dimensional electron holes, *Phys. Plasmas*, *15*, 112,901–+, doi:10.1063/1.3013452.
- Bougeret, J.-L., et al. (1995), Waves: The Radio and Plasma Wave Investigation on the Wind Spacecraft, *Space Science Reviews*, *71*, 231–263, doi:10.1007/BF00751331.

- Brice, N. (1964), Fundamentals of Very Low Frequency Emission Generation Mechanisms, *J. Geophys. Res.*, *69*, 4515–+, doi:10.1029/JZ069i021p04515.
- Cairns, I. H., and B. F. McMillan (2005), Electron acceleration by lower hybrid waves in magnetic reconnection regions, *Phys. Plasmas*, *12*, 102,110–+, doi:10.1063/1.2080567.
- Cattell, C., J. Crumley, J. Dombeck, J. R. Wygant, and F. S. Mozer (2002a), Polar observations of solitary waves at the Earth’s magnetopause, *Geophys. Res. Lett.*, *29*, 050,000–1, doi:10.1029/2001GL014046.
- Cattell, C., et al. (2002b), FAST observations of discrete electrostatic waves in association with down-going ion beams in the auroral zone, *J. Geophys. Res.*, *107*, 1238–+, doi:10.1029/2001JA000254.
- Cattell, C., C. Neiman, J. Dombeck, J. Crumley, J. Wygant, C. A. Kletzing, W. K. Peterson, F. S. Mozer, and M. André (2003), Large amplitude solitary waves in and near the Earth’s magnetosphere, magnetopause and bow shock: Polar and Cluster observations, *Nonlinear Processes in Geophysics*, *10*, 13–26.
- Cattell, C., et al. (2005), Cluster observations of electron holes in association with magnetotail reconnection and comparison to simulations, *J. Geophys. Res.*, *110*, 1211–+, doi:10.1029/2004JA010519.
- Coroniti, F. V. (1985), Space plasma turbulent dissipation - Reality or myth?, *Space Sci. Rev.*, *42*, 399–410, doi:10.1007/BF00214995.
- Davidson, R. C., and N. T. Gladd (1975), Anomalous transport properties associated with the lower-hybrid-drift instability, *Phys. Fluids*, *18*, 1327–1335, doi:10.1063/1.861021.
- Desch, M. (2005), Wind: Understanding Interplanetary Dynamics, nASA Goddard Space Flight Center, Online: <http://istp.gsfc.nasa.gov/wind.shtml>.
- Dum, C. T., R. Chodura, and D. Biskamp (1974), Turbulent Heating and Quenching of the Ion Sound Instability, *Phys. Rev. Lett.*, *32*, 1231–1234, doi:10.1103/PhysRevLett.32.1231.
- Dyrud, L. P., and M. M. Oppenheim (2006), Electron holes, ion waves, and anomalous resistivity in space plasmas, *J. Geophys. Res.*, *111*, 1302–+, doi:10.1029/2004JA010482.
- Ergun, R. E., C. W. Carlson, J. P. McFadden, F. S. Mozer, L. Muschietti, I. Roth, and R. J. Strangeway (1998a), Debye-Scale Plasma Structures Associated with Magnetic-Field-Aligned Electric Fields, *Phys. Rev. Lett.*, *81*, 826–829, doi:10.1103/PhysRevLett.81.826.
- Ergun, R. E., et al. (1998b), FAST satellite observations of large-amplitude solitary structures, *Geophys. Res. Lett.*, *25*, 2041–2044, doi:10.1029/98GL00636.
- Fairfield, D. H., and W. C. Feldman (1975), Standing waves at low Mach number laminar bow shocks, *J. Geophys. Res.*, *80*, 515–522, doi:10.1029/JA080i004p00515.

- Farris, M. H., C. T. Russell, and M. F. Thomsen (1993), Magnetic structure of the low beta, quasi-perpendicular shock, *J. Geophys. Res.*, *98*, 15,285–+, doi:10.1029/93JA00958.
- Fitzenreiter, R. J., K. W. Ogilvie, S. D. Bale, and A. F. Viñas (2003), Modification of the solar wind electron velocity distribution at interplanetary shocks, *J. Geophys. Res.*, *108*, 1415–+, doi:10.1029/2003JA009865.
- Franz, J. R., P. M. Kintner, and J. S. Pickett (1998), POLAR observations of coherent electric field structures, *Geophys. Res. Lett.*, *25*, 1277–1280, doi:10.1029/98GL50870.
- Franz, J. R., P. M. Kintner, C. E. Seyler, J. S. Pickett, and J. D. Scudder (2000), On the perpendicular scale of electron phase-space holes, *Geophys. Res. Lett.*, *27*, 169–+, doi:10.1029/1999GL010733.
- Franz, J. R., P. M. Kintner, J. S. Pickett, and L.-J. Chen (2005), Properties of small-amplitude electron phase-space holes observed by Polar, *J. Geophys. Res.*, *110*, 9212–+, doi:10.1029/2005JA011095.
- Fuselier, S. A., and D. A. Gurnett (1984), Short wavelength ion waves upstream of the earth’s bow shock, *J. Geophys. Res.*, *89*, 91–103, doi:10.1029/JA089iA01p00091.
- Gary, S. P., and M. M. Mellott (1985), Whistler damping at oblique propagation - Laminar shock precursors, *J. Geophys. Res.*, *90*, 99–104, doi:10.1029/JA090iA01p00099.
- Gloeckler, G., et al. (1995), The Solar Wind and Suprathermal Ion Composition Investigation on the Wind Spacecraft, *Space Science Reviews*, *71*, 79–124, doi:10.1007/BF00751327.
- Greenstadt, E. W., F. L. Scarf, C. T. Russell, V. Formisano, and M. Neugebauer (1975), Structure of the quasi-perpendicular laminar bow shock, *J. Geophys. Res.*, *80*, 502–514, doi:10.1029/JA080i004p00502.
- Gurnett, D. A., F. M. Neubauer, and R. Schwenn (1979a), Plasma wave turbulence associated with an interplanetary shock, *J. Geophys. Res.*, *84*, 541–552, doi:10.1029/JA084iA02p00541.
- Gurnett, D. A., E. Marsch, W. Pilipp, R. Schwenn, and H. Rosenbauer (1979b), Ion acoustic waves and related plasma observations in the solar wind, *J. Geophys. Res.*, *84*, 2029–2038, doi:10.1029/JA084iA05p02029.
- Hess, R. A., R. J. MacDowall, B. Goldstein, M. Neugebauer, and R. J. Forsyth (1998), Ion acoustic-like waves observed by ULYSSES near interplanetary shock waves in the three-dimensional heliosphere, *J. Geophys. Res.*, *103*, 6531–+, doi:10.1029/97JA03395.
- Hoppe, M. M., C. T. Russell, T. E. Eastman, and L. A. Frank (1982), Characteristics of the ULF waves associated with upstream ion beams, *J. Geophys. Res.*, *87*, 643–650, doi:10.1029/JA087iA02p00643.

- Huba, J. D., N. T. Gladd, and K. Papadopoulos (1978), Lower-hybrid-drift wave turbulence in the distant magnetotail, *J. Geophys. Res.*, *83*, 5217–5226, doi:10.1029/JA083iA11p05217.
- Hubbard, R. F., and T. J. Birmingham (1978), Electrostatic emissions between electron gyroharmonics in the outer magnetosphere, *J. Geophys. Res.*, *83*, 4837–4850, doi:10.1029/JA083iA10p04837.
- Kellogg, P. J. (1962), Flow of Plasma around the Earth, *J. Geophys. Res.*, *67*, 3805–+, doi:10.1029/JZ067i010p03805.
- Kellogg, P. J. (2003), Langmuir waves associated with collisionless shocks; a review, *Planet. Space Sci.*, *51*, 681–691.
- Kellogg, P. J., K. Goetz, S. J. Monson, and S. D. Bale (1999), A search for Langmuir solitons in the Earth’s foreshock, *J. Geophys. Res.*, *104*, 6751–6758, doi:10.1029/1999JA900021.
- Kennel, C. F., and H. E. Petschek (1966), Limit on stably trapped particle fluxes, *J. Geophys. Res.*, *71*, 1–28.
- Krasnoselskikh, V. V., V. V. Lobzin, K. Musatenko, J. Soucek, J. S. Pickett, and I. H. Cairns (2007), Beam-plasma interaction in randomly inhomogeneous plasmas and statistical properties of small-amplitude Langmuir waves in the solar wind and electron foreshock, *J. Geophys. Res.*, *112*, 10,109–+, doi:10.1029/2006JA012212.
- Lemons, D. S., and S. P. Gary (1978), Current-driven instabilities in a laminar perpendicular shock, *J. Geophys. Res.*, *83*, 1625–1632, doi:10.1029/JA083iA04p01625.
- Lepping, R. P., et al. (1995), The Wind Magnetic Field Investigation, *Space Science Reviews*, *71*, 207–229, doi:10.1007/BF00751330.
- Lin, R. P., et al. (1995), A Three-Dimensional Plasma and Energetic Particle Investigation for the Wind Spacecraft, *Space Science Reviews*, *71*, 125–153, doi:10.1007/BF00751328.
- Lu, Q. M., B. Lembege, J. B. Tao, and S. Wang (2008), Perpendicular electric field in two-dimensional electron phase-holes: A parameter study, *J. Geophys. Res.*, *113*, 11,219–+, doi:10.1029/2008JA013693.
- Lyons, L. R., R. M. Thorne, and C. F. Kennel (1972), Pitch-angle diffusion of radiation belt electrons within the plasmasphere., *J. Geophys. Res.*, *77*, 3455–3474, doi:10.1029/JA077i019p03455.
- Marsch, E., and T. Chang (1982), Lower hybrid waves in the solar wind, *Geophys. Res. Lett.*, *9*, 1155–1158, doi:10.1029/GL009i010p01155.
- Marsch, E., and T. Chang (1983), Electromagnetic lower hybrid waves in the solar wind, *J. Geophys. Res.*, *88*, 6869–6880, doi:10.1029/JA088iA09p06869.

- Matsukiyo, S., and M. Scholer (2006), On microinstabilities in the foot of high Mach number perpendicular shocks, *J. Geophys. Res.*, *111*, 6104–+, doi:10.1029/2005JA011409.
- Matsumoto, H., H. Kojima, T. Miyatake, Y. Omura, M. Okada, I. Nagano, and M. Tsutsui (1994), Electrotastic Solitary Waves (ESW) in the magnetotail: BEN wave forms observed by GEOTAIL, *Geophys. Res. Lett.*, *21*, 2915–2918, doi:10.1029/94GL01284.
- Mellott, M. M. (1985), Subcritical collisionless shock waves, *Geophys. Mono. Ser.*, *35*, 131–140.
- Mellott, M. M., and E. W. Greenstadt (1984), The structure of oblique subcritical bow shocks - ISEE 1 and 2 observations, *J. Geophys. Res.*, *89*, 2151–2161, doi:10.1029/JA089iA04p02151.
- Meyer-Vernet, N., and C. Perche (1989), Tool kit for antennae and thermal noise near the plasma frequency, *J. Geophys. Res.*, *94*, 2405–2415, doi:10.1029/JA094iA03p02405.
- Morton, K. W. (1964), Finite Amplitude Compression Waves in a Collision-Free Plasma, *Phys. Fluids*, *7*, 1800–1815.
- Ogilvie, K. W., et al. (1995), SWE, A Comprehensive Plasma Instrument for the Wind Spacecraft, *Space Sci. Rev.*, *71*, 55–77, doi:10.1007/BF00751326.
- Omura, Y., N. Furuya, and D. Summers (2007), Relativistic turning acceleration of resonant electrons by coherent whistler mode waves in a dipole magnetic field, *J. Geophys. Res.*, *112*, 6236–+, doi:10.1029/2006JA012243.
- Owens, A., et al. (1995), A High-Resolution GE Spectrometer for Gamma-Ray Burst Astronomy, *Space Science Reviews*, *71*, 273–296, doi:10.1007/BF00751333.
- Pickett, J. S., et al. (2004), Solitary waves observed in the auroral zone: the Cluster multi-spacecraft perspective, *Nonlinear Processes in Geophysics*, *11*, 183–196.
- Pulupa, M., and S. D. Bale (2008), Structure on Interplanetary Shock Fronts: Type II Radio Burst Source Regions, *Astrophys. J.*, *676*, 1330–1337, doi:10.1086/526405.
- Pulupa, M. P., S. D. Bale, and J. C. Kasper (2010), Langmuir waves upstream of interplanetary shocks: Dependence on shock and plasma parameters, *J. Geophys. Res.*, *115*, 4106–+, doi:10.1029/2009JA014680.
- Santolík, O., J. S. Pickett, D. A. Gurnett, J. D. Menietti, B. T. Tsurutani, and O. Verkhoglyadova (2010), Survey of Poynting flux of whistler mode chorus in the outer zone, *J. Geophys. Res.*, *115*, 0–+, doi:10.1029/2009JA014925.
- Shimada, N., and M. Hoshino (2000), Strong Electron Acceleration at High Mach Number Shock Waves: Simulation Study of Electron Dynamics, *Astrophys. J.*, *543*, L67–L71, doi:10.1086/318161.

- Soucek, J., V. Krasnoselskikh, T. Dudok de Wit, J. Pickett, and C. Kletzing (2005), Nonlinear decay of foreshock Langmuir waves in the presence of plasma inhomogeneities: Theory and Cluster observations, *J. Geophys. Res.*, *110*, 8102–+, doi:10.1029/2004JA010977.
- Stasiewicz, K., M. Longmore, S. Buchert, P. K. Shukla, B. Lavraud, and J. Pickett (2003), Properties of fast magnetosonic shocklets at the bow shock, *Geophys. Res. Lett.*, *30*, 240,000–1, doi:10.1029/2003GL017971.
- Storey, L. R. O. (1953), An Investigation of Whistling Atmospherics, *Royal Society of London Philosophical Transactions Series A*, *246*, 113–141.
- Stringer, T. E. (1963), Low-frequency waves in an unbounded plasma, *Journal of Nuclear Energy*, *5*, 89–107, doi:10.1088/0368-3281/5/2/304.
- Thomsen, M. F., J. T. Gosling, S. J. Bame, and M. M. Mellott (1985), Ion and electron heating at collisionless shocks near the critical Mach number, *J. Geophys. Res.*, *90*, 137–148, doi:10.1029/JA090iA01p00137.
- Usui, H., W. R. Paterson, H. Matsumoto, L. A. Frank, M. Nakamura, H. Matsui, T. Yamamoto, O. Nishimura, and J. Koizumi (1999), Geotail electron observations in association with intense bursts of electron cyclotron harmonic waves in the dayside magnetosphere, *J. Geophys. Res.*, *104*, 4477–4484, doi:10.1029/1998JA900151.
- Williams, J. D., L.-J. Chen, W. S. Kurth, D. A. Gurnett, M. K. Dougherty, and A. M. Rymer (2005), Electrostatic solitary structures associated with the November 10, 2003, interplanetary shock at 8.7 AU, *Geophys. Res. Lett.*, *32*, 17,103–+, doi:10.1029/2005GL023079.
- Wilson III, L. B., C. A. Cattell, P. J. Kellogg, K. Goetz, K. Kersten, L. Hanson, R. MacGregor, and J. C. Kasper (2007), Waves in Interplanetary Shocks: A Wind/WAVES Study, *Phys. Rev. Lett.*, *99*, 041,101–+, doi:10.1103/PhysRevLett.99.041101.
- Wilson III, L. B., C. A. Cattell, P. J. Kellogg, K. Goetz, K. Kersten, J. C. Kasper, A. Szabo, and K. Meziane (2009), Low-frequency whistler waves and shocklets observed at quasi-perpendicular interplanetary shocks, *J. Geophys. Res.*, *114*, 10,106–+, doi:10.1029/2009JA014376.
- Wilson III, L. B., C. A. Cattell, P. J. Kellogg, J. R. Wygant, K. Goetz, A. Breneman, and K. Kersten (2010a), A statistical study of the properties of large amplitude whistler waves and their association with few eV to 30 keV electron distributions observed in the magnetosphere by Wind, *J. Geophys. Res.*, submitted.
- Wilson III, L. B., C. A. Cattell, P. J. Kellogg, K. Goetz, K. Kersten, J. C. Kasper, A. Szabo, and M. Wilber (2010b), Large amplitude electrostatic waves observed at a supercritical interplanetary shock, *J. Geophys. Res.*, doi:10.1029/2010JA015332, in press.

Zhang, Y., and H. Matsumoto (1998), Magnetic noise bursts near the interplanetary shock associated with the coronal mass ejection event on February 21, 1994: The Geotail observations, *J. Geophys. Res.*, *103*, 20,561–20,580, doi:10.1029/98JA01234.